nature materials

Article

https://doi.org/10.1038/s41563-023-01585-2

Spontaneous orbital polarization in the nematic phase of FeSe

Received: 26 July 2022

Accepted: 19 May 2023

Published online: 22 June 2023

Check for updates

Connor A. Occhialini[1,3], Joshua J. Sanchez[1,3], Qian Song[1], Gilberto Fabbris[2], Yongseong Choi[2], Jong-Woo Kim[2], Philip J. Ryan[2] & Riccardo Comin[1]

The origin of nematicity in FeSe remains a critical outstanding question towards understanding unconventional superconductivity in proximity to nematic order. To understand what drives the nematicity, it is essential to determine which electronic degree of freedom admits a spontaneous order parameter independent from the structural distortion. Here we use X-ray linear dichroism at the Fe K pre-edge to measure the anisotropy of the 3*d* orbital occupation as a function of in situ applied stress and temperature across the nematic transition. Along with using X-ray diffraction to precisely quantify the strain state, we reveal a lattice-independent, spontaneously ordered orbital polarization within the nematic phase, as well as an orbital polarizability that diverges as the transition is approached from above. These results provide strong evidence that spontaneous orbital polarization serves as the primary order parameter of the nematic phase.

Symmetry-breaking phase transitions in strongly correlated electron systems are characterized by their structural and electronic (spin, charge and orbital) degrees of freedom[1]. In electronically ordered phases, these degrees of freedom become intertwined, making an experimental determination of the leading interaction challenging. One striking example of this complex interplay is nematicity, an electronically driven rotational symmetry breaking that is widely observed in iron-based superconductors[2]. While static nematic order is found to compete with superconductivity in iron pnictide materials such as Co-doped $BaFe_2As_2$ (refs. 2–4), it may actually help stabilize superconductivity in the chalcogenide FeSe (ref. 5). Thus, understanding the origin of nematic order in each class is essential for understanding the nature of superconductivity[6]. Despite sustained efforts, a persistent question is whether nematicity is driven by the spin or orbital degree of freedom, the answer to which has remained elusive due to the complexity of the microscopic relationship between the degrees of freedom and the nematicity-induced structural anisotropy.

The central difficulty in addressing the orbital degree of freedom arises from its close association with the lattice symmetry. This problem is important not just to nematicity in iron-based superconductors, but also to phenomena as diverse as Jahn–Teller distortions in transition-metal oxides[1,7] and quadrupolar 4*f* ordering in heavy fermion materials[8,9]. In this work, we introduce a general methodology to distinguish the orbital and lattice degrees of freedom by combining in situ tunable strain with X-ray linear dichroism (XLD) and X-ray diffraction (XRD), to directly probe the orbital polarization and strain state of the lattice, respectively. We use this methodology to provide the most direct evidence that orbital ordering drives the nematic transition in the iron-based superconductor FeSe.

FeSe displays a nematic transition at $T_s = 90$ K, which results in a small lattice orthorhombicity and a large anisotropy in both orbital occupation and spin fluctuations, as demonstrated by many techniques[10–20]. While elastoresistivity measurements have identified an electronic driver for the nematic transition[16,21–24], this technique alone cannot uniquely identify the driving interaction[25,26]. The primary role of the orbital degree of freedom in the nematic phase has been suggested by nuclear magnetic resonance (NMR)[10,12] and angle-resolved photoemission spectroscopy (ARPES)[13–16] measurements that reveal anisotropy between the Fe $|3d_{xz}\rangle$ and $|3d_{yz}\rangle$ orbitals. Meanwhile, nematicity in the iron pnictide materials is widely thought to result as a vestigial order of antiferromagnetism[2], and spin-driven nematic fluctuations likely play a major role in the enhancement of superconductivity. However, this spin-nematic model for FeSe is fundamentally challenged by the absence of long-range antiferromagnetic order and by the preservation of nematic order while spin fluctuations are suppressed below the superconducting transition temperature[11,12].

[1]Department of Physics, Massachusetts Institute of Technology, Cambridge, MA, USA. [2]Advanced Photon Source, Argonne National Laboratory, Lemont, IL, USA. [3]These authors contributed equally: Connor A. Occhialini, Joshua J. Sanchez. e-mail: rcomin@mit.edu

https://doi.org/10.1038/s41563-023-01585-2

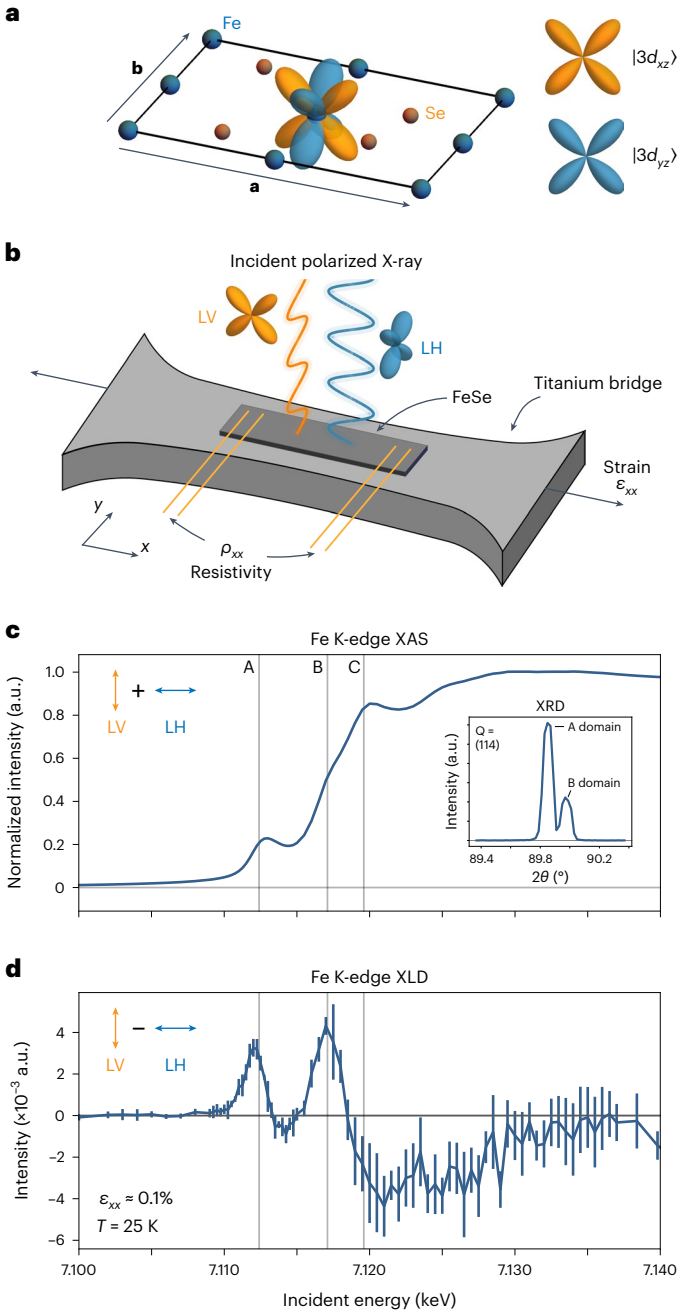

Fig. 1 | Strain apparatus and XLD spectroscopy in FeSe. a, The orthorhombic unit cell of FeSe, defining the **a** and **b** orthorhombic axes and the orientation of the $|3d_{xz}\rangle$ and $|3d_{yz}\rangle$ orbitals (A domain). **b**, Schematic of the strain apparatus and sample, with polarization states (LH or LV) for normal incidence dichroism measurements. **c**, Sample 1, the Fe K-edge XAS profile at $T = 25$ K under tension ($\epsilon_{xx} \approx 0.1\%$). The inset shows the XRD intensity of the (114) reflection vs diffraction angle, revealing partial detwinning towards the A domain. **d**, The corresponding XLD spectrum with error bars determined from the standard deviation of repeated scans ($n = 5$; Methods).

Intriguingly, these strong spin fluctuations may nonetheless be key to the enhancement of superconductivity while having only a minimal or subdominant role in the formation of nematic order[27].

The investigation of nematicity is challenging due to the presence of structural twin domains, which form below the nematic transition and cause bulk probes to average out the electronic anisotropy. Several recent works have used fixed applied strain to (partially or fully) detwin the nematic domains and probe the spin or orbital anisotropy[18,20,28]. However, a fixed-strain methodology cannot assess the nature of the coupling between the lattice and electronic degrees of freedom, which is key for understanding what drives the system into a nematic state. Furthermore, any strain applied above the transition induces anisotropy where there is none spontaneously, while within the ordered phase, any excess strain applied beyond full detwinning will increase the anisotropy beyond the spontaneous value. Thus, it is necessary to observe the behaviour of the electronic anisotropy as a function of both strain and temperature across the nematic transition[29,30].

Here, we address this question using strain-dependent XLD at the Fe K pre-edge to probe the local orbital degree of freedom at the Fe site and determine the Fe 3*d* orbital polarization in the nematic state. We use in situ tunable applied stress to precisely detwin the structural domains and further strain the lattice. These XLD measurements, along with supporting XRD measurements to quantify the strain state, allow us to determine a robust relationship between the orbital and lattice degrees of freedom as a function of strain and temperature across the nematic phase boundary. A key result of this work is the observation of a saturating XLD signal beyond full detwinning in the nematic phase. This suggests a spontaneously ordered orbital polarization that serves as a primary nematic order parameter, analogous to a saturating magnetization in a ferromagnet. Further, both the strain susceptibility of the orbital polarization (the orbital polarizability) and the simultaneously measured elastoresistivity diverge on approach to the transition from above, consistent with local nematic fluctuations driven by the orbital degree of freedom. While these measurements do not address the spin degree of freedom directly, the transport measurements reveal a secondary source of resistivity anisotropy attributed to anisotropic scattering by spin fluctuations, which is activated only below T_s and is enhanced with increasing orthorhombicity in a strain regime where the orbital polarization is saturated. These measurements thus isolate the critical role of the orbital degree of freedom in the nematic phase of FeSe and provide direct evidence that nematicity is primarily driven by orbital order.

X-ray absorption and XLD spectra in detwinned FeSe

We performed measurements on two samples from the same crystal growth batch. The crystals were cut into rectangular bars with edges parallel to the orthorhombic **a** and **b** directions (Supplementary Fig. 1). The samples were then mounted on a titanium support platform as described in the literature[23,31] and fit with transport leads in a four-wire geometry for determining the longitudinal resistivity ρ_{xx} along the applied stress direction (Fig. 1b). Uniaxial stress was applied to the platform with a Razorbill CS130 strain cell, with the nominal strain ϵ_{xx} determined by the capacitance strain gauge on the stress device (Methods).

Sample 1 was initially cooled to temperature $T = 25$ K under moderate tensile stress ($\epsilon_{xx} \approx 0.1\%$), which partially detwins the structural domains that form below T_s. We define the structural A domain (B domain) as that with the longer **a** (shorter **b**) lattice constant aligned parallel to the stress axis (Fig. 1a). The inset to Fig. 1c shows an XRD measurement of the (114) reflection, revealing a 75% detwinning state, in agreement with the predicted detwinning given the 0.23% orthorhombicity. Figure 1c shows the Fe K-edge X-ray absorption spectra (XAS), taken at normal incidence with incident linear horizontal (LH) or vertical (LV) polarizations (parallel to **a** or **b** in the tensionally detwinned state, respectively) and normalized to the main edge jump (Methods). The near-edge structure shows three features labelled A, B or C, consistent with previous studies[32–34]. We report the associated in-plane XLD spectrum in Fig. 1d, defined as the difference of the LV and LH intensities, $I_{LV} - I_{LH}$ (further XLD characterization is in Supplementary Figs. 2–4).

The Fe K-edge resonance results from dipole-allowed transitions from Fe 1*s* to Fe 4*p* states, with admixed Fe 3*d* and Se 4*p*/4*d* orbital character due to hybridization. Feature B is the usual main edge of this

https://doi.org/10.1038/s41563-023-01585-2

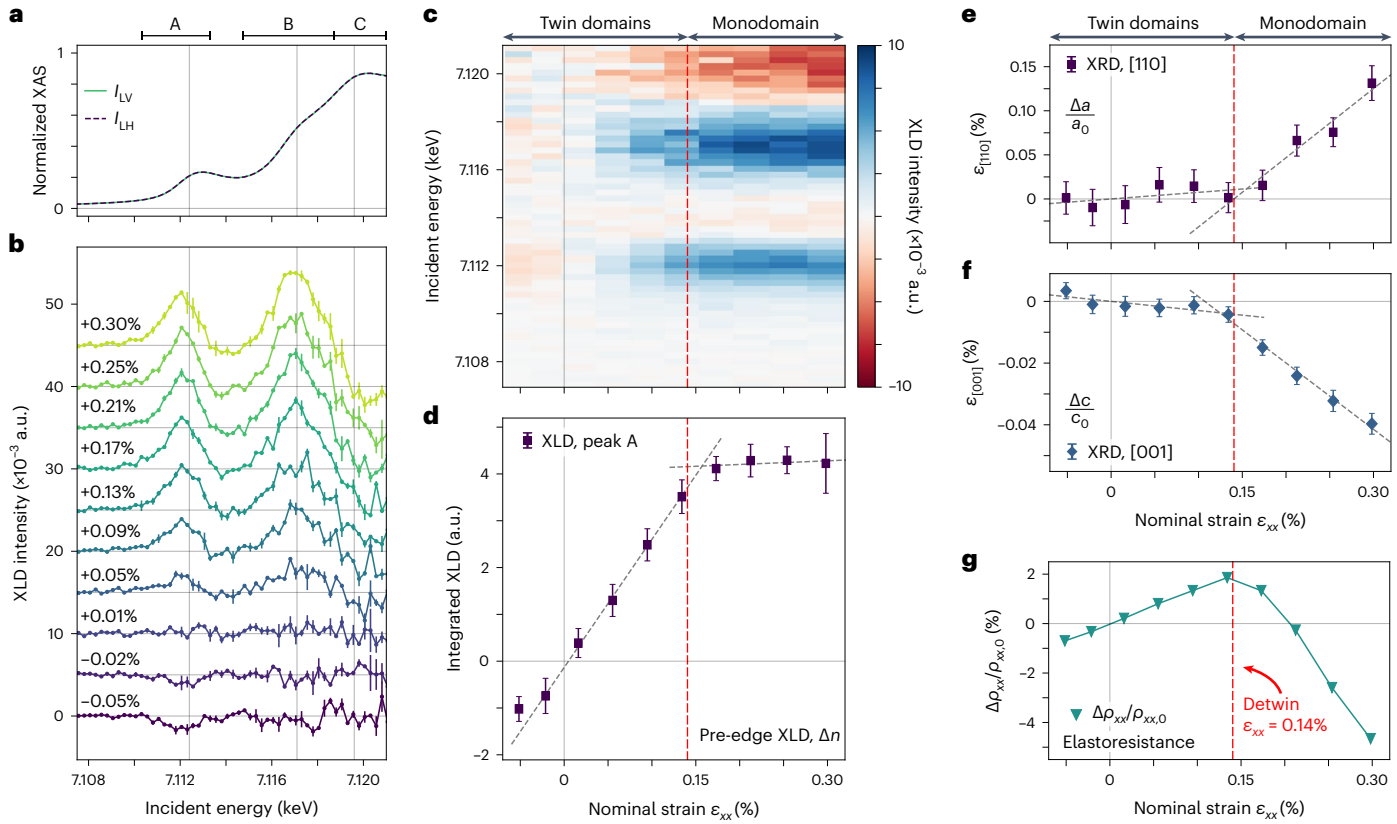

Fig. 2 | Strain-dependent X-ray measurements in the nematic phase. X-ray measurements versus strain on sample 1 at $T = 50$ K. **a**, The Fe K-edge XAS profile for polarizations LH ∥ **a** and LV ∥ **b**, with the integration regions for the features A, B and C noted. **b**, In-plane XLD spectra as a function of increasing strain from −0.05% (bottom) to 0.30% (top). Error bars represent the standard deviation of repeated scans ($n = 2$). **c**, Colour map of the strain-dependent in-plane XLD spectra in **b**. **d**, The integrated XLD intensity of the pre-edge A (Δn) as a function of applied strain with error bars corresponding to propagated error from the XLD spectra in **b**. **e**,**f**, XRD measurements of the [110] direction (**e**; parallel to applied strain) and [001] direction (**f**; out of plane) lattice strains versus nominal linear strain ϵ_{xx}. Error bars represent the standard error from Gaussian fits to XRD peaks. **g**, Elastoresistance measurements ($\rho_{xx}/\rho_{xx,0}$ vs ϵ_{xx}, where $\rho_{xx,0}$ is the zero-strain value) recorded simultaneously with XLD and XRD data, showing a sign reversal at the detwinning point, $\epsilon_{xx} \approx 0.14\%$, denoted by the vertical red dashed lines in panels **c**–**g**. All measurements reported in **a**–**g** are taken at identical strain conditions.

transition[32,33]. Higher incident energies (peak C) are dominated by non-local effects including multiple scattering and encode Fe 4*p* and Se 4*d* hybridization. Thus, feature C is sensitive to the Fe–Se bond length and long-range structural distortions[33,34]. A lower incident energy favours increasingly local electronic states around the absorbing Fe atom[35,36], and the pre-edge (peak A) coincides with the unoccupied Fe 3*d* density of states near the Fermi level. Due to the local tetrahedral symmetry, the $|3d_{xz}\rangle$ ($|3d_{yz}\rangle$) orbital exhibits strong on-site hybridization with $|4p_y\rangle$ ($|4p_x\rangle$) states[37–40], giving access to 3*d* orbitals through dipole transitions at the pre-edge (Supplementary Figs. 5–8). In this picture, the positive pre-edge XLD in the tensionally detwinned state (Fig. 1d) corresponds to a more occupied $|3d_{yz}\rangle$ state (Fig. 1a), in agreement with the Γ-point occupation anisotropy seen in ARPES[13,14,28].

Spontaneous orbital polarization

We now discuss the simultaneously recorded XLD, XRD and elastoresistivity data collected at fixed strain values on a compressive-to-tensile strain sweep in sample 1 at $T = 50$ K (Methods). Figure 2a–d shows the XLD spectra as a function of strain. The XLD intensity at each XAS feature is strain tunable and reverses sign between compression and tension, consistent with the detwinning of nematic domains. The integrated XLD intensity of the pre-edge peak is plotted versus strain in Fig. 2d. The XLD value increases rapidly before saturating at larger strain, with the saturation occurring near $\epsilon_{xx} \approx 0.14\%$.

On the same strain loop, we used XRD to measure the strain response of the A domain's **a** and **c** lattice constants, from which we determine the unidirectional strains $\Delta a/a_0$ and $\Delta c/c_0$ shown in Fig. 2e,f, where a_0 and c_0 are the zero-strain values of the lattice constants. The lattice constants exhibit a weak response to small strain before changing rapidly at large tensile strain, indicating a detwinning strain of $\epsilon_{xx} \approx 0.14\%$, denoted by red vertical lines in Fig. 2. Thus, strains below the detwinning point act to reorient nematic domains with only a negligible effect on the lattice constants of an individual domain[41]. The assignment of the detwinning point is corroborated by the disappearance of the B domain twin peak at the (114) reflection (Supplementary Figs. 9 and 10). The crossover in the monodomain lattice response is also concomitant with a sign change in the slope of the simultaneously measured resistivity (Fig. 2g), discussed in more detail in the following.

We thus find that the saturation of the pre-edge XLD coincides with the full detwinning of the sample. By contrast, the higher energy XLD features continue to increase with tension past the detwinning point (Fig. 2b,c and Supplementary Fig. 4). This suggests that the higher energy XLD features probe the net lattice anisotropy between the $\hat{x}$ and $\hat{y}$ directions (Fig. 1b), which changes with both detwinning and strain-enhanced orthorhombicity. Indeed, the structural contributions to the XLD are linear in the orthorhombicity and well-captured by multiple scattering calculations[42] (Supplementary Figs. 5–7). From these considerations, we conclude that the saturating pre-edge XLD signature (with integrated value Δn) corresponds to a lattice-independent, spontaneous polarization of Fe 3*d* orbitals that is only weakly coupled to further structural distortion.

https://doi.org/10.1038/s41563-023-01585-2

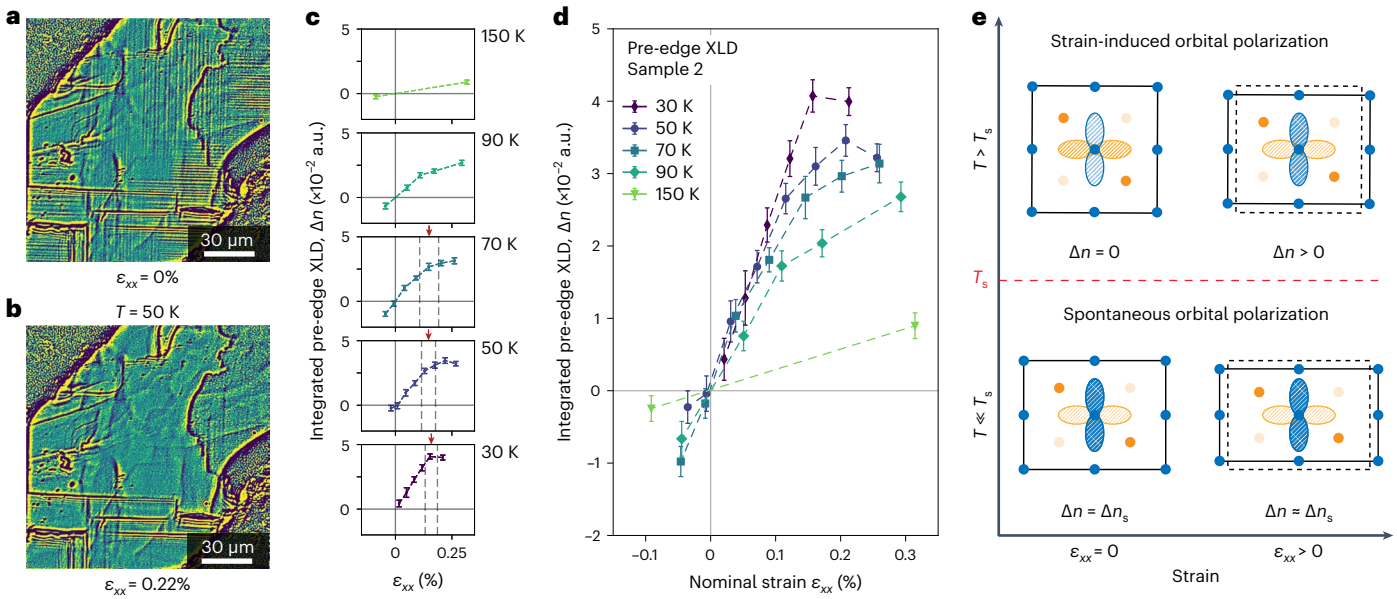

Fig. 3 | Spontaneous orbital polarization across the nematic transition. **a**,**b**, Optical birefringence images of the nematic domains at $T = 50$ K on sample 2 at $\epsilon_{xx} = 0\%$ (**a**) and $\epsilon_{xx} = 0.22\%$ (**b**) strain showing the full detwinning. Scale bars are 30 μm. **c**, Temperature- and strain-dependent pre-edge XLD measurements (Δn) across the nematic transition in sample 2. For $T < T_s$, the approximate detwinning points are indicated by red arrows, determined from independent XRD and optical birefringence measurements (Methods and Supplementary Figs. 11 and 12). Vertical dashed grey lines indicate the range of uncertainty in the detwinning point. **d**, The same data in **c** plotted together to highlight the temperature dependence and strain dependence. XLD error bars are as defined in Figs. 1 and 2. **e**, Above the nematic transition ($T > T_s$, top), the orbital polarization is only non-zero with applied strain. Far below the nematic transition ($T \ll T_s$, bottom), the orbital polarization is spontaneously non-zero with a fully saturated value Δn_s that is unchanged with applied strain beyond full detwinning, indicating it is not driven by the lattice distortion.

To further associate the orbital polarization with the emergence of nematicity, we performed XLD measurements on sample 2 as a function of strain and at fixed temperatures above and below the nematic transition. We plot Δn versus strain in Fig. 3c,d. At a given tensile strain value, Δn clearly increases with decreasing temperature, while at a given temperature the susceptibility is maximum near zero strain. Using a combination of XRD and optical birefringence measurements (Supplementary Figs. 11 and 12), we identify the approximate detwinning strain point at each temperature below T_s, which coincides with the inflection point of Δn. These data indicate an orbital polarization that develops with decreasing temperature below T_s with a diminishing strain susceptibility beyond full detwinning (Supplementary Fig. 13).

Finally, we characterized the orbital polarizability above the nematic transition in sample 1. To do so, we measured the temperature dependence of Δn at a moderate fixed tensile strain of $\epsilon_{xx} \approx 0.2\%$ (Fig. 4a). The constant linear strain state is confirmed by XRD measurements, and a fixed orthorhombicity is suggested by the constancy of peak C in the XLD spectrum between 120 K and 90 K, which encodes the structural orthorhombicity (Supplementary Fig. 14). Over this same temperature range, the peak A XLD (Δn) increases strongly (over a factor of two) before saturating for $T < T_s$. This is quantified with a Curie–Weiss analysis for $T > T_s$, revealing a Curie temperature $T^* = 62.5 \pm 5$ K (Fig. 4a), thus identifying a divergence of Δn as T_s is approached from above. Since this divergence occurs under fixed lattice conditions, we understand Δn as originating from a strain alignment of diverging orbital-origin nematic fluctuations and not as a secondary orbital response to the lattice distortion. Below T_s, the XLD signal appears to be nearly saturated, even up to the transition itself, which is due to both domain detwinning and additional strain-induced orbital polarization. This demonstrates that a fixed-strain methodology cannot capture the continuous onset of the spontaneous order parameter, which instead requires a fixed-temperature variable-strain approach as in Figs. 2 and 3.

The combined strain dependence and temperature dependence reveals two distinct pieces of evidence regarding the nature of the measured orbital polarization. On one hand, the strain-dependent curves as a function of temperature directly show that a lattice-independent, spontaneously ordered orbital polarization emerges in the nematic phase (Fig. 3e, top). At the same time, the strain susceptibility of the orbital polarization shows a divergence under fixed-strain conditions above T_s (Fig. 3e, bottom). This behaviour is reminiscent of the magnetization across a paramagnetic to ferromagnetic transition, with the magnetic field being replaced by an antisymmetric strain as the poling field, and associates the orbital polarization with the primary order parameter of the nematic phase. Therefore, the effect of strain far below the transition is only to reorient 'nematic moments' that are fixed in magnitude and orientationally locked to the underlying structure. Evidence for such a scenario is supported by X-ray pair distribution function experiments[43], which associate local nematic moments with a short-range-ordered orbital degeneracy lifting that persists far above the nematic transition, consistent with the temperature dependence and strain dependence above T_s in our experiments.

Signatures of orthorhombicity-coupled spin fluctuations

These conclusions are further supported by simultaneous elastoresistivity measurements, which reveal a close correspondence between the orbital polarization and the resistivity anisotropy above T_s that breaks down within the nematic phase. In Fig. 4b, we show the temperature-dependent elastoresistance collected simultaneously with the fixed-strain XLD measurements (Fig. 4a). Above T_s, the resistivity anisotropy ($\Delta\rho_{xx}/\rho_{xx,0}$, where $\rho_{xx,0}$ is the zero-strain value) diverges with a Curie–Weiss temperature dependence towards $T^* \approx 61.4 \pm 3.1$ K, consistent with previous elastoresistivity measurements[23,44] and in close correspondence to the Curie temperature of Δn ($T^* = 62.5 \pm 5$ K).

https://doi.org/10.1038/s41563-023-01585-2

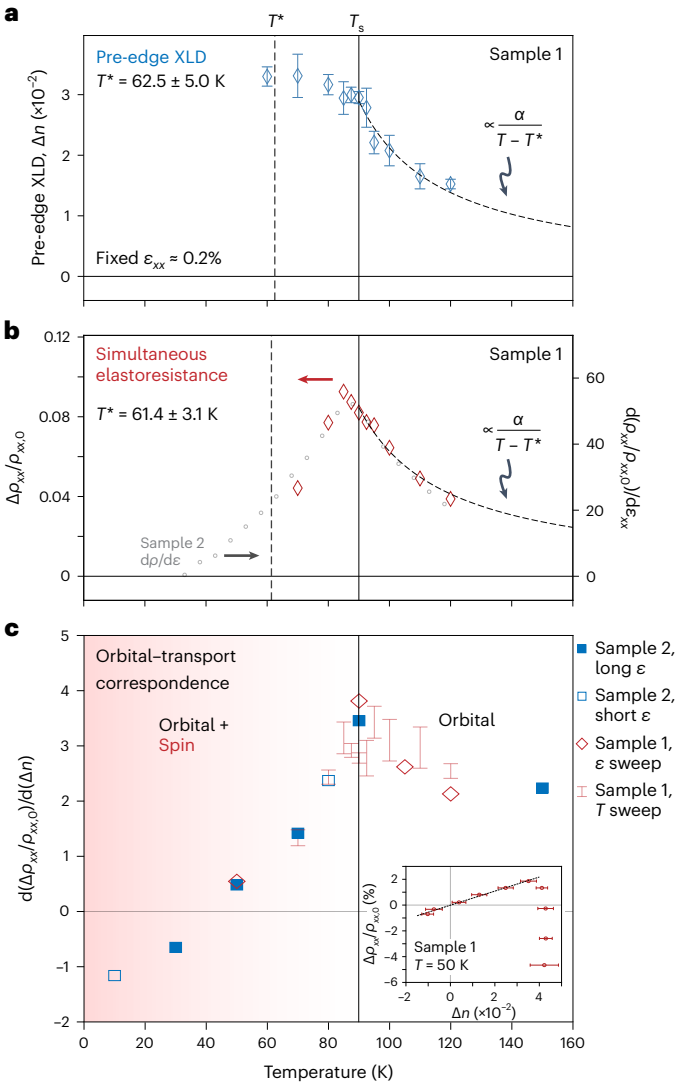

Fig. 4 | Divergent orbital polarizability and orbital–transport correspondence. a,**b**, The Δn (**a**) and the simultaneous elastoresistance (**b**; red diamonds, left axis) versus temperature across T_s at a fixed $\varepsilon_{xx} \approx 0.2\%$ for sample 1. Dashed curves are Curie–Weiss fits to the data at $T \geq T_s = 90$ K, indicating Curie–Weiss temperatures of $T^* \approx 62.5 \pm 5$ K and 61.4 ± 3 K, respectively. Also shown in **b** is the longitudinal elastoresistivity coefficient about zero strain in sample 2 (grey circles, right axis; Supplementary Fig. 11) for comparison. **c**, Ratio of the normalized resistivity to the pre-edge XLD measurement versus temperature, taken from the slope of the linear fit of normalized resistivity at $T = 50$ K (inset), additional temperatures in sample 1 (Supplementary Fig. 17, red diamonds), equivalent data from sample 2 (Fig. 3c and Supplementary Figs. 16 and 18, blue squares) and the fixed-strain temperature sweep in sample 1 (Fig. 4a,b, red bars). The pink shading indicates the growing influence of the spin degree of freedom on the transport below the nematic transition. The inset shows the normalized resistivity versus XLD in sample 1 at $T = 50$ K using data from Fig. 2d,g. Error bars in **a** and **c** are determined from the statistical errors of the XLD signal, and are the size of the data point where not indicated.

Below T_s, Δn saturates while $\Delta\rho_{xx}/\rho_{xx,0}$ decreases rapidly, implying a breakdown in the orbital–transport correspondence.

This is highlighted in more detail in Fig. 4c (inset), where we plot $\Delta\rho_{xx}/\rho_{xx,0}$ versus Δn from Fig. 2d,g for sample 1 at $T = 50$ K (Supplementary Figs. 15–18). Here the resistivity increases linearly with the orbital polarization up to the detwinning point, beyond which it decreases rapidly with increasing strain even while the XLD value remains saturated. Equivalent data in sample 2 show the same orbital–transport linearity up to full detwinning, with a strongly temperature-dependent proportionality (Supplementary Fig. 16). In Fig. 4c we plot the slope of $\Delta\rho_{xx}/\rho_{xx,0}$ versus Δn from both samples across temperature and phase, for both fixed-strain temperature sweeps and fixed-temperature strain sweeps within the detwinning strain regime (Supplementary Figs. 15–18). We find a positive and weakly temperature-dependent orbital–transport proportionality above T_s, which rapidly diminishes below the transition, with a sign change near $T = 40$ K. Taken together, these results suggest a second source of elastoresistivity that becomes dominant only below T_s and at strains beyond full detwinning.

The elastoresistivity encodes information from several distinct but ultimately intertwined sources: orbital polarization primarily creates anisotropy in the Drude weight, while spin fluctuations primarily create anisotropy in the scattering rate[22,25,26,45–47]. Thus, orbital and spin contributions to the elastoresistivity can behave independently. Our simultaneous XLD and transport measurements enable us to show that the resistivity has a component that closely corresponds to the orbital polarization, both above T_s and within the detwinning strain regime below T_s. We propose that the second component of the elastoresistivity originates from spin scattering. FeSe exhibits the same stripe-type spin fluctuations as those found in iron pnictide materials[10,12,17,18,20], which are thought to drive the large negative elastoresistivity in the latter. In the non-magnetically ordered nematic phase of FeSe, a strain-enhanced orthorhombicity is expected to enhance the anisotropy of the spin fluctuations[24,48] and their effect on transport anisotropy[30,46], reflecting the propensity of the system to undergo a putative stripe-type magnetic transition. This then can explain both the decreasing magnitude of the elastoresistivity below T_s as well as the distinct proportionality in the detwinning and post-detwinning strain regimes (Supplementary Fig. 11). A strain–transport study of FeSe using a more direct probe of spin fluctuations with a tunable strain state would be needed to confirm this scenario.

Discussion

Due to the intertwined nature of spin and orbital degrees of freedom, two general routes have been invoked to explain the nematicity in FeSe. In the spin-nematic picture, divergent orbital-selective spin fluctuations drive the nematic ordering and consequently induce a splitting between the $|3d_{xz}\rangle$ and $|3d_{yz}\rangle$ bands. Our observation of (1) a large nematic-phase spontaneous orbital polarization, (2) its divergence behaviour above T_s and (3) the direct correspondence between the orbital polarization and the transport anisotropy above T_s overall suggests that nematicity is instead driven by orbital order.

In this case, the increasing Fermi surface anisotropy below T_s enhances strongly anisotropic spin fluctuations (as evidenced by our elastoresistivity analysis), which can themselves act as a mechanism for a further momentum-dependent evolution of the Fermi surface[13,45,49]. The change of the Fermi surface topology and orbital content at the hole and electron pockets observed by ARPES[13,14], the associated suppression of B_{1g} charge fluctuations in Raman measurements[19,50], the increase of the spin-relaxation rate in NMR[12], the abrupt sign change in the Hall coefficient[24,51] and the unusual sign-changing elastoresistivity[16,21,24], all manifesting only below T_s, may be the clearest signs of this effect. This sequence of events, where orbital-dependent spin fluctuations are triggered below T_s by the onset of nematicity driven by spontaneous orbital order, may reconcile the apparently disparate conclusions reached by previous studies and is consistent with our experimental observations. Indeed, inelastic neutron scattering has shown that the spin frustration between Néel order (with C_4 rotational symmetry) and stripe-type order (with C_2 rotational symmetry) is partially lifted by the nematic transition and its accompanying orthorhombic structural distortion[52]. Thus, our proposed notion of orthorhombicity-stabilized spin fluctuations is consistent with the available experimental evidence from more direct probes of the spin degrees of freedom[17,18,20,52], although additional data using the tunable

strain methodology introduced here are required to assess how spin fluctuations modulate the properties of the orbital nematic state.

Finally, several observations stand as key indicators that nematicity and superconductivity are driven by distinct degrees of freedom in FeSe. Below the onset of superconductivity, spin fluctuations are diminished for both Co-doped $BaFe_2As_2$ (ref. 4) and FeSe (refs. 12,17), but the orthorhombicity is suppressed only for the former[3] while being apparently unaffected in the latter[11]. Furthermore, optimal superconductivity is not found in the vicinity of the nematic quantum critical point in FeSe under hydrostatic pressure[53] or S doping[21,27], in contrast to the iron pnictides. This may be naturally understood in our interpretation of orbital nematicity, as this regime of the phase diagram does not then correspond to the critical spin fluctuations thought to drive the unconventional pairing in the pnictides[2]. Instead, the presence of an orbital nematic state may affect other aspects of superconductivity in FeSe, including the anisotropy of the superconducting gap and the orbital dependence of the pairing state[5,54]. These results disentangle spin fluctuations from nematicity in FeSe, and thus allow a refocusing towards the more relevant part of the phase diagram for optimizing chalcogenide superconductivity.

Online content

Any methods, additional references, Nature Portfolio reporting summaries, source data, extended data, supplementary information, acknowledgements, peer review information; details of author contributions and competing interests; and statements of data and code availability are available at https://doi.org/10.1038/s41563-023-01585-2.

References

1. Khomskii, D. I. *Transition Metal Compounds* (Cambridge Univ. Press, 2014).
2. Si, Q., Yu, R. & Abrahams, E. High-temperature superconductivity in iron pnictides and chalcogenides. *Nat. Rev. Mater.* **1**, 16017 (2016).
3. Nandi, S. et al. Anomalous suppression of the orthorhombic lattice distortion in superconducting $Ba(Fe_{1-x}Co_x)_2As_2$ single crystals. *Phys. Rev. Lett.* **104**, 057006 (2010).
4. Pratt, D. K. et al. Coexistence of competing antiferromagnetic and superconducting phases in the underdoped $Ba(Fe_{0.953}Co_{0.047})_2As_2$ compound using X-ray and neutron scattering techniques. *Phys. Rev. Lett.* **103**, 087001 (2009).
5. Liu, D. et al. Orbital origin of extremely anisotropic superconducting gap in nematic phase of FeSe superconductor. *Phys. Rev. X* **8**, 031033 (2018).
6. Chen, X., Maiti, S., Fernandes, R. M. & Hirschfeld, P. J. Nematicity and superconductivity: competition versus cooperation. *Phys. Rev. B* **102**, 184512 (2020).
7. Wilkins, S. B. et al. Direct observation of orbital ordering in $La_{0.5}Sr_{1.5}MnO_4$ using soft X-ray diffraction. *Phys. Rev. Lett.* **91**, 167205 (2003).
8. Willers, T. et al. Correlation between ground state and orbital anisotropy in heavy fermion materials. *Proc. Natl Acad. Sci. USA* **112**, 2384–2388 (2015).
9. Rosenberg, E. W., Chu, J. H., Ruff, J. P., Hristov, A. T. & Fisher, I. R. Divergence of the quadrupole-strain susceptibility of the electronic nematic system $YbRu_2Ge_2$. *Proc. Natl Acad. Sci. USA* **116**, 7232–7237 (2019).
10. Li, J. et al. Spin-orbital-intertwined nematic state in FeSe. *Phys. Rev. X* **10**, 011034 (2020).
11. Böhmer, A. E. et al. Lack of coupling between superconductivity and orthorhombic distortion in stoichiometric single-crystalline FeSe. *Phys. Rev. B* **87**, 180505 (2013).
12. Baek, S. H. et al. Orbital-driven nematicity in FeSe. *Nat. Mater.* **14**, 210–214 (2015).
13. Pfau, H. et al. Momentum dependence of the nematic order parameter in iron-based superconductors. *Phys. Rev. Lett.* **123**, 066402 (2019).
14. Yi, M. et al. Nematic energy scale and the missing electron pocket in FeSe. *Phys. Rev. X* **9**, 041049 (2019).
15. Shimojima, T. et al. Lifting of *xz*/*yz* orbital degeneracy at the structural transition in detwinned FeSe. *Phys. Rev. B* **90**, 121111 (2014).
16. Watson, M. D. et al. Emergence of the nematic electronic state in FeSe. *Phys. Rev. B Condens. Matter Mater. Phys.* **91**, 155106 (2015).
17. Wang, Q. et al. Strong interplay between stripe spin fluctuations, nematicity and superconductivity in FeSe. *Nat. Mater.* **15**, 159–163 (2016).
18. Chen, T. et al. Anisotropic spin fluctuations in detwinned FeSe. *Nat. Mater.* **18**, 709–716 (2019).
19. Massat, P. et al. Charge-induced nematicity in FeSe. *Proc. Natl Acad. Sci. USA* **113**, 9177–9181 (2016).
20. Lu, X. et al. Spin-excitation anisotropy in the nematic state of detwinned FeSe. *Nat. Phys.* **18**, 806–812 (2022).
21. Hosoi, S. et al. Nematic quantum critical point without magnetism in $FeSe_{1-x}S_x$ superconductors. *Proc. Natl Acad. Sci. USA* **113**, 8139–8143 (2016).
22. Tanatar, M. A. et al. Origin of the resistivity anisotropy in the nematic phase of FeSe. *Phys. Rev. Lett.* **117**, 127001 (2016).
23. Bartlett, J. M. et al. Relationship between transport anisotropy and nematicity in FeSe. *Phys. Rev. X* **11**, 021038 (2021).
24. Ghini, M. et al. Strain tuning of nematicity and superconductivity in single crystals of FeSe. *Phys. Rev. B* **103**, 205139 (2021).
25. Chinotti, M., Pal, A., Degiorgi, L., Böhmer, A. E. & Canfield, P. C. Ingredients for the electronic nematic phase in FeSe revealed by its anisotropic optical response. *Phys. Rev. B* **98**, 094506 (2018).
26. Schütt, M., Schmalian, J. & Fernandes, R. M. Origin of DC and AC conductivity anisotropy in iron-based superconductors: scattering rate versus spectral weight effects. *Phys. Rev. B* **94**, 075111 (2016).
27. Baek, S. H. et al. Separate tuning of nematicity and spin fluctuations to unravel the origin of superconductivity in FeSe. *npj Quantum Mater.* **5**, 8 (2020).
28. Huh, S. S. et al. Absence of Y-pocket in 1-Fe Brillouin zone and reversed orbital occupation imbalance in FeSe. *Commun. Phys.* **3**, 52 (2020).
29. Cai, C. et al. Momentum-resolved measurement of electronic nematic susceptibility in the $FeSe_{0.9}S_{0.1}$ superconductor. *Phys. Rev. B* **101**, 180501 (2020).
30. Fernandes, R. M., Böhmer, A. E., Meingast, C. & Schmalian, J. Scaling between magnetic and lattice fluctuations in iron pnictide superconductors. *Phys. Rev. Lett.* **111**, 137001 (2013).
31. Park, J. et al. Rigid platform for applying large tunable strains to mechanically delicate samples. *Rev. Sci. Instrum.* **91**, 083902 (2020).
32. Lebert, B. W., Balédent, V., Toulemonde, P., Ablett, J. M. & Rueff, J. P. Emergent high-spin state above 7 GPa in superconducting FeSe. *Phys. Rev. B* **97**, 180503 (2018).
33. Joseph, B. et al. A study of the electronic structure of $FeSe_{1-x}Te_x$ chalcogenides by Fe and Se K-edge X-ray absorption near edge structure measurements. *J. Phys. Condens. Matter* **22**, 485702 (2010).
34. Simonelli, L. et al. Electronic properties of $FeSe_{1-x}Te_x$ probed by X-ray emission and absorption spectroscopy. *J. Phys. Condens. Matter* **24**, 415501 (2012).
35. De Groot, F., Vankó, G. & Glatzel, P. The 1s X-ray absorption pre-edge structures in transition metal oxides. *J. Phys. Condens. Matter* **21**, 104207 (2009).

36. Modrow, H., Bucher, S., Rehr, J. J. & Ankudinov, A. L. Calculation and interpretation of K-shell X-ray absorption near-edge structure of transition metal oxides. *Phys. Rev. B* **67**, 035123 (2003).
37. de Figueiredo, A. G. et al. Orbital localization and the role of the Fe and As 4*p* orbitals in $BaFe_2As_2$ probed by XANES. *Phys. Rev. B* **105**, 045130 (2022).
38. Chen, J. M. et al. Electronic structure and characteristics of Fe 3*d* valence states of $Fe_{1.01}Se$ superconductors under pressure probed by X-ray absorption spectroscopy and resonant X-ray emission spectroscopy. *J. Chem. Phys.* **137**, 244702 (2012).
39. Yamamoto, T. Assignment of pre-edge peaks in K-edge X-ray absorption spectra of 3d transition metal compounds: electric dipole or quadrupole? *X-ray Spectrom.* **37**, 572–584 (2008).
40. Lee, C. C., Yin, W. G. & Ku, W. Ferro-orbital order and strong magnetic anisotropy in the parent compounds of iron-pnictide superconductors. *Phys. Rev. Lett.* **103**, 267001 (2009).
41. Sanchez, J. J. et al. The transport–structural correspondence across the nematic phase transition probed by elasto X-ray diffraction. *Nat. Mater.* **20**, 1519–1524 (2021).
42. Chen, C. C. et al. Orbital order and spontaneous orthorhombicity in iron pnictides. *Phys. Rev. B* **82**, 100504 (2010).
43. Koch, R. J. et al. Room temperature local nematicity in FeSe superconductor. *Phys. Rev. B* **100**, 020501 (2019).
44. Ishida, K. et al. Pure nematic quantum critical point accompanied by a superconducting dome. *Proc. Natl Acad. Sci. USA* **119**, e2110501119 (2022).
45. Fanfarillo, L. et al. Orbital-dependent Fermi surface shrinking as a fingerprint of nematicity in FeSe. *Phys. Rev. B* **94**, 155138 (2016).
46. Onari, S. & Kontani, H. In-plane anisotropy of transport coefficients in electronic nematic states: universal origin of nematicity in Fe-based superconductors. *Phys. Rev. B* **96**, 094527 (2017).
47. Fernandes, R. M., Abrahams, E. & Schmalian, J. Anisotropic in-plane resistivity in the nematic phase of the iron pnictides. *Phys. Rev. Lett.* **107**, 217002 (2011).
48. He, M. et al. Evidence for short-range magnetic order in the nematic phase of FeSe from anisotropic in-plane magnetostriction and susceptibility measurements. *Phys. Rev. B* **97**, 104107 (2018).
49. Rhodes, L. C., Watson, M. D., Haghighirad, A. A., Evtushinsky, D. V. & Kim, T. K. Revealing the single electron pocket of FeSe in a single orthorhombic domain. *Phys. Rev. B* **101**, 235128 (2020).
50. Udina, M., Grilli, M., Benfatto, L. & Chubukov, A. V. Raman response in the nematic phase of FeSe. *Phys. Rev. Lett.* **124**, 197602 (2020).
51. Sun, J. P. et al. High-T_c superconductivity in FeSe at high pressure: dominant hole carriers and enhanced spin fluctuations. *Phys. Rev. Lett.* **118**, 147004 (2017).
52. Wang, Q. et al. Magnetic ground state of FeSe. *Nat. Commun.* **7**, 12182 (2016).
53. Sun, J. et al. Dome-shaped magnetic order competing with high-temperature superconductivity at high pressures in FeSe. *Nat. Commun.* **7**, 12146 (2016).
54. Hanaguri, T. et al. Two distinct superconducting pairing states divided by the nematic end point in $FeSe_{1-x}S_x$. *Sci. Adv.* **4**, eaar6419 (2018).

Methods

Sample preparation

Single crystals of FeSe with typical dimensions of 2.0 mm × 2.0 mm × 0.05 mm were grown using the KCl–ACl_3 flux method as described in ref. 17. The resulting samples were cut with a laser cutter with a wavelength λ = 1,064 nm (spot size of 10 µm) into rectangular bars with dimensions of 1.0 mm × 0.15 mm with the long axis along the tetragonal [110] (orthorhombic **a**) direction. The samples were then mounted onto prefabricated titanium platforms (following the specifications outlined in refs. 23,31) using Stycast 2850LT epoxy and cured at 80 °C for 12 hours. After the epoxy was cured, the sample surface was cleaved several times to reduce the thickness to ≈25 µm, and 25 µm gold wires were affixed near the ends of the long axis of the sample (Fig. 1b and Supplementary Fig. 1) in a four-wire geometry using Epotex H20E silver epoxy. The silver epoxy was cured in a nitrogen-filled glove box at 120 °C for 15 minutes for sample 2 and at 80 °C in ambient conditions for 2 hours for sample 1. The Ti platform with the wired FeSe bars was then fastened to a Razorbill CS130 strain cell.

XAS, XLD and XRD measurements

X-ray absorption and diffraction measurements were performed at the 4-ID-D endstation of the Advanced Photon Source, Argonne National Laboratory. The strain cell was mounted into an Advanced Research Systems Displex closed-cycled cryostat with a base temperature $T \approx 10$ K. The cryostat was mounted in a six-circle diffractometer to allow sample manipulation for XRD, as well as precise alignment of the incident beam to the surface normal of the sample for in-plane XLD measurements. XAS spectra were recorded in partial fluorescence yield at the Fe Kα emission line in a quasi-backscattering geometry with a Hitachi Vortex detector. The incident energy was varied across the Fe K-edge resonance, and at each incident energy, the polarization was rapidly switched between linear polarization states using diamond phase plates in the sequence LV/LH/LH/LV in order to determine the linear dichroism spectrum with a high signal-to-noise ratio.

All reported XAS spectra were normalized to the main edge jump using reference XAS/XLD spectra acquired up to 7.140 keV. The reported XLD value was calculated as the direct difference of the normalized XAS spectra at different polarizations. For the high-statistics near-edge XLD spectra used for Figs. 2 and 3, two to three spectra were acquired back to back and averaged, in the energy range of 7.107–7.121 keV with a step size of 250 meV. The standard deviation of these subsequent scans was used for the error bars of the XLD data. XRD measurements were performed with an incidence energy above the Fe K-edge resonance, with an energy of 7.200 keV and 7.400 keV for sample 1 and sample 2, respectively. The X-ray measurements were performed with a beam size of 50 × 50 μm^2 and were bulk sensitive, and thus averaged over multiple twin domains when present[22] (Fig. 3a,b).

Strain–temperature sweep procedures

All data reported were taken by sweeping the voltage of the piezo stacks of the strain device continuously from maximum compression to maximum tension. Before changing temperature, the voltage on the piezo stacks was fixed to zero. This ensured a consistent nominal zero-strain capacitance reading throughout the experiment. Once at the target temperature, the sample would be initialized by moving to maximum tension and then back to maximum compression before initializing the sweep. This consistent initialization procedure accounts for any effects of detwinning hysteresis or hysteretic effects of the piezo-actuators or Ti bridge, ensuring consistent and comparable strain-dependent measurements throughout the experiment. We further note that as we directly control the total length of the sample via applying stress to the titanium platform, we do not directly observe hysteresis in the detwinning process, in contrast to the methodology involving a sample suspended over a gap as in ref. 41.

For the strain sweep data in Fig. 2, the sample was initialized with the above procedure at T = 50 K, and strain was increased monotonically from maximum compression to tension. At each strain point, XAS and XLD spectra at normal incidence and XRD measurements of the (114) and (004) reflections were performed at an identical strain condition before moving to the next increased tensile strain point. The resistivity values were stable at fixed strains, and the reported resistance values were averaged over the duration of corresponding XLD measurements.

For the XLD temperature dependence recorded in sample 2 (Fig. 3), the measurements were completed from the same, single cool down of the cryostat, starting at low temperature (10 K) and increasing monotonically to the highest measured temperature (150 K). Reported resistance measurements were again averaged over the duration of the XLD measurements, and thus the reported quantities are under identical strain conditions. XRD measurements were also performed in sample 2. These were performed on subsequent strain loops at the same temperature conditions, immediately after the XLD/resistance strain loops. The sample was consistently initialized, and separate strain sweeps following the same compressive-to-tensile strain loop as the XLD measurements were repeated for separate measurements of the (114) and (004) reflections.

Determination of nominal strain

All reported data are plotted versus nominal linear strain ϵ_{xx}. For XLD measurements, the nominal zero strain was determined by the capacitance read-out of the strain cell gap corresponding to the interpolated value for zero XLD signal, signalling a fully twinned sample below T_s, or an unstrained tetragonal phase above (Supplementary Fig. 15). Since XLD is bulk sensitive, this provides the most consistent measure of the true zero-strain value. The conversion of the change in the strain cell gap distance with respect to this zero, monitored by the change in the capacitance across the gap, was determined by strain transmission data at T = 90 K of the [110] lattice parameter, calculated from the combined XRD values of the (114) and (004) reflections. The temperature T = 90 K was chosen for strain transmission data since the lack of orthorhombic domains results in a linear strain transmission, as opposed to the highly nonlinear effects observed within the nematic phase (Fig. 2e,f) due to details of the detwinning process.

Optical birefringence measurements

Optical birefringence and additional elastoresistivity data were acquired on sample 2 with identical sample preparation conditions (no change in the strain cell, mounting or wiring). Polarized images were acquired using a monochrome camera with a broadband light-emitting diode light source that was passed through a λ = 600 nm long-pass filter (ThorLabs) in order to increase the birefringence contrast[22]. The incident light was polarized with a broadband Glan–Thompson polarizer (Thorlabs) along the tetragonal [100] direction (bisection of the orthorhombic axes). To resolve the birefringence-induced polarization rotation, another Glan–Thompson polarizer was placed before the camera and detuned by ≈1° from the cross-polarized configuration (with respect to the polarizer) in order to optimize the birefringent domain contrast. The images were recorded using both ×20 and ×50 objectives (Olympus).

Data availability

Data associated with this paper are available on the Harvard Dataverse at https://doi.org/10.7910/DVN/SGZVX7.

Acknowledgements

We thank R. Fernandes, M. Norman, J. Analytis, M. Le Tacon, J. Pelliciari, E. Ergeçen, Q. Jiang, P. Malinowski, M. Bachmann, M. Yi and H. Pfau for discussions. We thank L. G. Pimenta Martins and Y. Lee for assistance with preliminary X-ray experiments.

Work at MIT (C.A.O., J.J.S., Q.S. and R.C.) is supported by the Department of Energy, Office of Science, Office of Basic Energy Sciences, under Award Number DE-SC0019126 (resonant X-ray spectroscopy and diffraction measurements, and sample growth), by the Air Force Office of Scientific Research Young Investigator Program under grant FA9550-19-1-0063 (strain set-up development and transport measurements), and by the National Science Foundation under grant no. 1751739 (optical dichroism). The work performed at the Advanced Photon Source was supported by the US Department of Energy, Office of Science, Office of Basic Energy Sciences under contract no. DE-AC02-06CH11357. Sample preparation was performed in part at HPCAT (Sector 16) at the Advanced Photon Source, Argonne National Laboratory. J.J.S. acknowledges the support of the National Science Foundation MPS-Ascend Postdoctoral Research Fellowship under award no. 2138167. Any opinions, findings and conclusions or recommendations expressed in this material are those of the author(s) and do not necessarily reflect the views of the National Science Foundation.

Author contributions

C.A.O., J.J.S., G.F., Y.C., J.-W.K. and P.J.R. conceived the project and performed all X-ray measurements. Q.S. grew the samples. C.A.O. and J.J.S. prepared the samples for strain measurements, performed the optical birefringence measurements, analysed the data and wrote the manuscript. All authors contributed to the discussion of the results and commented on the manuscript. R.C. supervised the project.

Competing interests

The authors declare no competing interests.

Additional information

Supplementary information The online version contains supplementary material available at https://doi.org/10.1038/s41563-023-01585-2.

Correspondence and requests for materials should be addressed to Riccardo Comin.

Peer review information *Nature Materials* thanks the anonymous reviewers for their contribution to the peer review of this work.